# Field-Singularity Correction in 2-D Time-Domain Haar-Wavelet Modeling of Waveguide Components

Masafumi Fujii, *Member, IEEE,* and Wolfgang J. R. Hoefer, *Fellow, IEEE*

***Abstract*—A time-domain Haar-wavelet-based modeling technique has been applied to two-dimensional waveguide problems including discontinuities. The field singularity at discontinuities such as edges and corners of conductors is corrected by quasi-static field approximation. Combination of quasi-static correction and wavelet modeling significantly improves the computational efficiency compared to conventional time-domain analysis techniques. The proposed technique was applied to waveguides perturbed by thin and thick irises and also iris-coupled waveguide filters. The computational efficiency of the technique is demonstrated by examining the convergence of the results obtained with different discretizations.**

***Index Terms*—Electromagnetic-field analysis, field-singularity correction, Haar wavelets, time domain.**

## I. Introduction

WAVELET theory has been introduced to time-domain formulation of electromagnetic-field analysis [1], [2] to increase computational efficiency and accuracy compared to conventional algorithms. It has been reported that wavelet basis functions allow coarser discretization than the conventional space discrete methods because of the small numerical dispersion property when applied to the electromagnetic-field analysis. When thresholding techniques are included, wavelet-based methods acquire an adaptive grid capability, which is one of the most desirable features in solving differential equations.

However, there are two difficulties that must be overcome when using wavelets. One is a realization of complicated boundary conditions and the other is an implementation of a thresholding technique—both may significantly increase computational overhead. Several papers have been published to tackle these difficulties by employing mathematically more sophisticated wavelets such as Daubechies' compactly supported wavelets with two vanishing moments [3]–[5] and biorthogonal B-spline wavelets [6]. These techniques have advantages in specific applications. However, significant advantages over the conventional analysis techniques have not been achieved thus far in terms of versatility, accuracy, and computational efficiency.

Manuscript received March 25, 1999; revised August 12, 1999.

The authors are with the Department of Electrical and Computer Engineering, University of Victoria, Victoria, BC, Canada V8W 3P6 (e-mail: fujii@engr.uvic.ca).

Publisher Item Identifier S 0018-9480(01)02423-1.

In this paper, the time-domain Haar-wavelet-based (TD-Haar) modeling technique [7], [8] for the two-dimensional (2-D) TE waveguide mode has been formulated with a complete set of the 2-D Haar wavelets. Although Haar scaling and wavelet functions are simple rectangular functions, they have the following important features.

1) Haar wavelets are the only wavelets that are real, compactly supported, symmetric, and orthogonal.
2) This simplicity allows the modeling of complicated boundary conditions to be easier than other wavelet-based methods.
3) The minimum support property allows arbitrary spatial grid intervals, leading to a nonuniform grid scheme.

These features of Haar wavelets fit very well to the space-discrete analysis methods like the finite-difference scheme.

In order to apply the 2-D TD-Haar modeling technique to waveguide structures, the following various features have been implemented in this paper:

1) perfect electric conductor (PEC) and perfect magnetic conductor (PMC) conditions;
2) Berenger's perfectly matched layer (PML) absorbing boundary condition [9];
3) $90^\circ$ and $0^\circ$ corner node with field-singularity correction by means of quasi-static field approximation that was first applied to the finite-difference time-domain (FDTD) method by Mur [10].

The combination of Haar-wavelet modeling with the field-singularity correction technique considerably improves the computational performance; the field-singularity correction allows us to use coarser discretization. Moreover, the Haar-wavelet modeling improves accuracy, especially when the discretization is coarse and reduces the number of operation approximately by half [8], [11].

The TD-Haar modeling is first applied to a simple rectangular waveguide terminated with PML absorbing boundaries. This example conveys a clear understanding of the decomposition of the electromagnetic field in a waveguide, as well as the behavior of the wavelet basis in the analysis. The technique is then applied to the analysis of waveguides with thin and thick inductive irises and two types of iris-coupled waveguide filters. These applications demonstrate the adaptability of the field-singularity correction in a wavelet-based time-domain field-modeling technique.

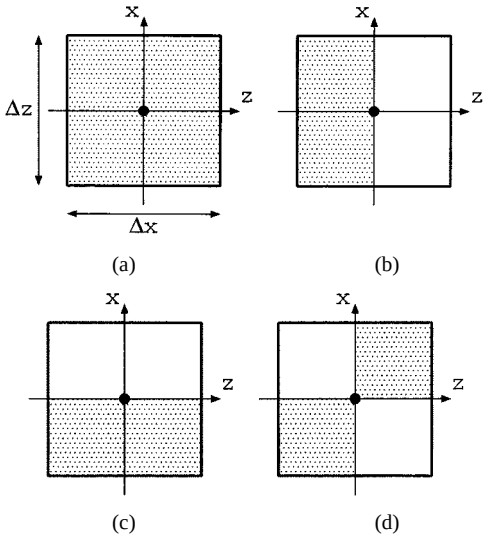


Fig. 1. 2-D Haar basis functions for an $E_y$ node. Hatched regions represent $+1$ and unhatched regions represent $-1$. (a) $\phi_i(x)\phi_k(z)$, (b) $\phi_i(x)\psi_k(z)$, (c) $\psi_i(x)\phi_k(z)$, (d) $\psi_i(x)\psi_k(z)$.

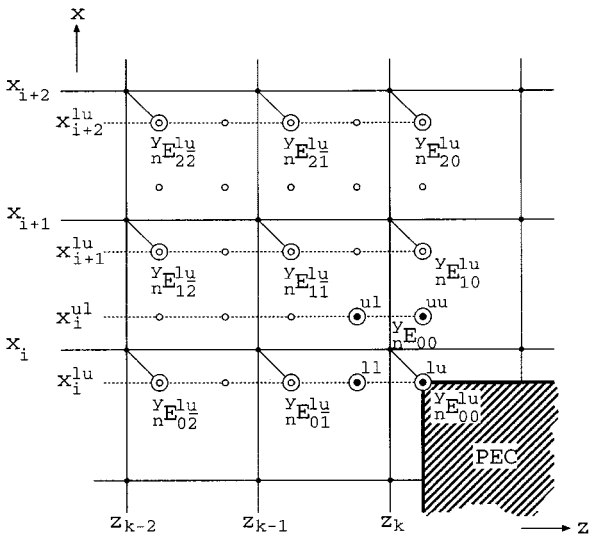


Fig. 2. Implementation of a 90° corner node at the "$lu$" sampling point of node $(i,\ k)$. Thin solid lines show the equivalent Yee grid. The hatched region shows a PEC.

## II. Formulation and Implementation

### A. 2-D Time Iterative Difference Equations

Maxwell's curl equations for the TE case

$$\frac{\partial E_y}{\partial x} = -\mu\frac{\partial H_z}{\partial t} \tag{1}$$

$$\frac{\partial E_y}{\partial z} = \mu\frac{\partial H_x}{\partial t} \tag{2}$$

$$\frac{\partial H_x}{\partial z} - \frac{\partial H_z}{\partial x} = \epsilon\frac{\partial E_y}{\partial t} + J_y + \sigma E_y \tag{3}$$

are discretized. The field variables $E_y$, $H_z$, and $H_x$ are first expanded by using the complete set of the 2-D Haar-wavelet basis functions shown in Fig. 1. Using the quantities that are defined by $E$ and $H$ fields multiplied by the grid intervals

$${}^{y}_{n}V_{i,k} \equiv {}^{y}_{n}E_{i,k} \tag{4}$$

$${}^{z}_{n+1/2}I_{i+1/2,k} \equiv {}_{n+1/2}H_{i+1/2,k}\Delta z \tag{5}$$

$${}^{x}_{n+1/2}I_{i,k+1/2} \equiv {}_{n+1/2}H_{i,k+1/2}\Delta x \tag{6}$$

and applying Galerkin's procedure to these components with Haar scaling and wavelet basis functions, we obtain time-stepping update equations of the following form [7], [8]:

$${}^{z}_{h}I_{h0} = {}^{z}_{\bar{h}}I_{h0} + C_{mz}({}^{y}_{0}V_{10} - {}^{y}_{0}V_{00}) \tag{7}$$

$${}^{x}_{h}I_{0h} = {}^{x}_{\bar{h}}I_{0h} + C_{mx}(-{}^{y}_{0}V_{01} + {}^{y}_{0}V_{00}) \tag{8}$$

$${}^{y}_{1}V_{00} = C_{00}{}^{y}_{0}V_{00} + C_e\cdot\left\{{}^{x}_{h}I_{0h} - {}^{x}_{\bar{h}}I_{0\bar{h}} - ({}^{z}_{h}I_{h0} - {}^{z}_{\bar{h}}I_{\bar{h}0}) - {}^{y}_{h}\hat{I}_{00}\right\} \tag{9}$$

where the updating coefficients with the material constants $\epsilon$, $\sigma$, and $\mu$ are given by

$$C_{mx} = -\frac{\Delta t}{\mu_{ik}}\cdot\left[\frac{\Delta x}{\Delta z}\right]_{ik} \tag{10}$$

$$C_{mz} = -\frac{\Delta t}{\mu_{ik}}\cdot\left[\frac{\Delta z}{\Delta x}\right]_{ik} \tag{11}$$

$$C_0 = \frac{2\epsilon_{ik} - \sigma_{ik}\Delta t}{2\epsilon_{ik} + \sigma_{ik}\Delta t} \tag{12}$$

$$C_e = \frac{2\Delta t}{2\epsilon_{ik} + \sigma_{ik}\Delta t}\cdot\left[\frac{1}{\Delta x\Delta z}\right]_{ik}. \tag{13}$$

The notations are simplified as ${}^{y}_{0}V_{10} \equiv {}^{y}_{n}V^{\xi\zeta}_{i+1,k}$, ${}^{z}_{\bar{h}}I_{h0} \equiv {}^{z}_{n-1/2}I^{\xi\zeta}_{i+1/2,k}$, etc., with the time interval $\Delta t$, time index $n$, space indexes $i$ and $k$, and wavelet and scaling functions $\xi$, $\zeta = \phi$ and $\psi$. Equations (7)–(9) are the same as in the conventional FDTD method, except that they are computed for the four individual basis functions $\xi\zeta = \phi\phi$, $\phi\psi$, $\psi\phi$, and $\psi\psi$ individually.

### B. PEC Edge and Corner Node

In order to model corners and edges of a conductor, special nodes are implemented to enforce the field near the corners and the edges to have a smooth field distribution. Furthermore, the singular fields around the corners and the edges are corrected by using quasi-static field approximation [10].

*1) 90° Corner Node:* Fig. 2 shows an example of a corner node at the "$lu$" sampling point. For the implementation of a 90° corner node, $E_y$ fields at the sampling points are calculated by interpolation from the peripheral field values. In Fig. 2, the $E_y$ fields at the corner node (noted with a black dot with a circle) are interpolated from the peripheral field values (noted with double circles). By using the second-order Lagrange interpolation, and considering that ${}^{y}_{n}E^{lu}_{00} = 0$ at the corner, the $E_y$ fields at the sampling points "$ll$," "$ul$," and "$uu$" are, respectively, given by

$${}^{y}_{n}E^{ll}_{00} = L_1{}^{y}_{n}E^{lu}_{0\bar{1}} + L_2{}^{y}_{n}E^{lu}_{0\bar{2}} \tag{14}$$

$${}^{y}_{n}E^{uu}_{00} = L_1{}^{y}_{n}E^{lu}_{10} + L_2{}^{y}_{n}E^{lu}_{20} \tag{15}$$

$$\begin{aligned}{}^{y}_{n}E^{ul}_{00} = {} & L_0\left(L_1{}^{y}_{n}E^{lu}_{0\bar{1}} + L_2{}^{y}_{n}E^{lu}_{0\bar{2}}\right) \\ & + L_1\left(L_0{}^{y}_{n}E^{lu}_{10} + L_1{}^{y}_{n}E^{lu}_{1\bar{1}} + L_2{}^{y}_{n}E^{lu}_{1\bar{2}}\right) \\ & + L_2\left(L_0{}^{y}_{n}E^{lu}_{20} + L_1{}^{y}_{n}E^{lu}_{2\bar{1}} + L_2{}^{y}_{n}E^{lu}_{2\bar{2}}\right)\end{aligned} \tag{16}$$

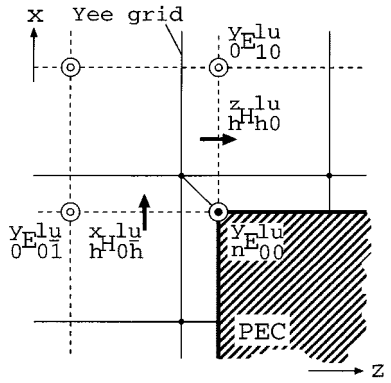


Fig. 3. 90° corner located at the "$lu$" sampling point

with the Lagrange polynomial coefficients

$$L_0\Big|_{x=x_i^{ul}} = \frac{(x-x_{i+1}^{lu})(x-x_{i+2}^{lu})}{(x_i^{lu}-x_{i+1}^{lu})(x_i^{lu}-x_{i+2}^{lu})}\Bigg|_{x=x_i^{ul}} = \frac{3}{8} \tag{17}$$

$$L_1\Big|_{x=x_i^{ul}} = \frac{(x-x_i^{lu})(x-x_{i+2}^{lu})}{(x_{i+1}^{lu}-x_i^{lu})(x_{i+1}^{lu}-x_{i+2}^{lu})}\Bigg|_{x=x_i^{ul}} = \frac{3}{4} \tag{18}$$

$$L_2\Big|_{x=x_i^{ul}} = \frac{(x-x_i^{lu})(x-x_{i+1}^{lu})}{(x_{i+2}^{lu}-x_i^{lu})(x_{i+2}^{lu}-x_{i+1}^{lu})}\Bigg|_{x=x_i^{ul}} = -\frac{1}{8}. \tag{19}$$

The Haar-basis coefficients at node $(i, k)$ are then obtained by the linear transformation

$$\begin{bmatrix} {}_n^yE_{ik}^{\phi\phi} \\ {}_n^yE_{ik}^{\phi\psi} \\ {}_n^yE_{ik}^{\psi\phi} \\ {}_n^yE_{ik}^{\psi\psi} \end{bmatrix} = \boldsymbol{A}_{2D} \begin{bmatrix} {}_n^yE_{ik}^{ll} \\ {}_n^yE_{ik}^{lu} \\ {}_n^yE_{ik}^{ul} \\ {}_n^yE_{ik}^{uu} \end{bmatrix} \tag{20}$$

where

$$\boldsymbol{A}_{2D} = \frac{1}{2}\begin{bmatrix} +1 & +1 & +1 & +1 \\ +1 & -1 & +1 & -1 \\ +1 & +1 & -1 & -1 \\ +1 & -1 & -1 & +1 \end{bmatrix}. \tag{21}$$

*2) Field-Singularity Correction at 90° Corners:* Following the discussion in [10], the implementation of the field-singularity correction at the corner of the "$lu$" sampling point (see Fig. 3) is given by

$$-{}_h^xI_{0\bar{h}}^{lu} = -{}_h^xI_{0\bar{h}}^{lu} + \frac{\Delta t}{\mu_0}\frac{\Delta x}{\Delta z}\nu_1 2^{1-\nu_1}\,{}_0^yV_{0\bar{1}}^{lu} \tag{22}$$

$$-{}_h^zI_{h0}^{lu} = -{}_h^zI_{h0}^{lu} + \frac{\Delta t}{\mu_0}\frac{\Delta z}{\Delta x}\nu_1 2^{1-\nu_1}\,{}_0^yV_{10}^{lu} \tag{23}$$

where $\nu_1 = \pi/(2\pi-(\pi/2)) = 2/3$, and the correction factor is $\nu_1 2^{1-\nu_1} = (2/3)2^{1/3} \approx 0.83994737$.

*3) 0° Edge Node:* The 0° edge node is implemented in a similar way as in the 90° corner node; it is slightly modified such that the fields at five sampling points around the edge are interpolated and corrected. For the edge node at the "$lu$" sampling point, shown in Fig. 4, additional fields at sampling points "$ul$" and "$ll$" of node $(i, k+1)$ are interpolated by

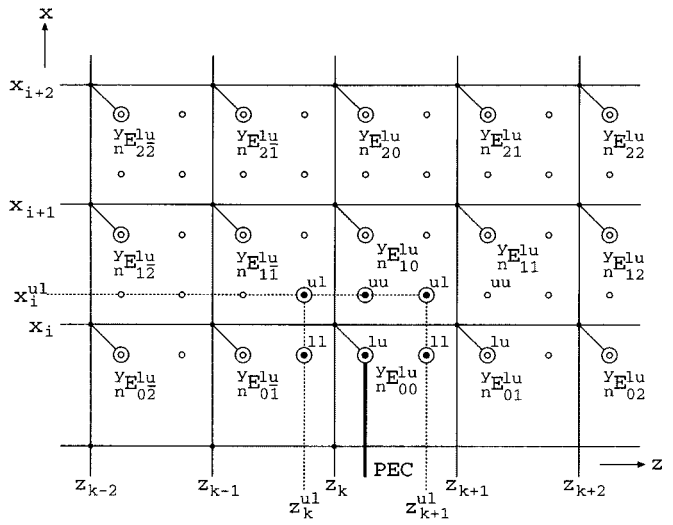


Fig. 4. Implementation of a 0° edge node at the "$lu$" sampling point of node $(i, k)$. Thin solid lines show the equivalent Yee grid.

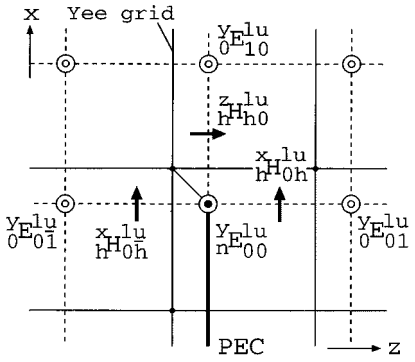


Fig. 5. 0° edge located at the "$lu$" sampling point.

$$\begin{aligned} {}_n^yE_{01}^{ll} &= L_1\,{}_n^yE_{01}^{lu} + L_2\,{}_n^yE_{02}^{lu} \qquad (24)\\ {}_n^yE_{01}^{ul} &= L_0\Big(L_1\,{}_n^yE_{01}^{lu} + L_2\,{}_n^yE_{02}^{lu}\Big) \\ &\quad + L_1\Big(L_0\,{}_n^yE_{10}^{lu} + L_1\,{}_n^yE_{11}^{lu} + L_2\,{}_n^yE_{12}^{lu}\Big) \\ &\quad + L_2\Big(L_0\,{}_n^yE_{20}^{lu} + L_1\,{}_n^yE_{21}^{lu} + L_2\,{}_n^yE_{22}^{lu}\Big) \qquad (25) \end{aligned}$$

where the Lagrange polynomial coefficients are given by (17)–(19). The above equations are calculated together with (14)–(16) and the resulting field distribution is converted to Haar basis coefficients by the linear transformation (20).

*4) Field-Singularity Correction at 0° Edges:* The field singularity at the 0° edge shown in Fig. 5 is given by

$${}_h^xI_{0h}^{lu} = {}_h^xI_{0h}^{lu} + \frac{\Delta t}{\mu_0}\frac{\Delta x}{\Delta z}\nu_1 2^{1-\nu_1}\,{}_0^yV_{01}^{lu} \tag{26}$$

together with (22) and (23), where $\nu_1 = 1/2$ and the correction factor is $\nu_1 2^{1-\nu_1} = (1/2)2^{1/2} \approx 0.70710678$.

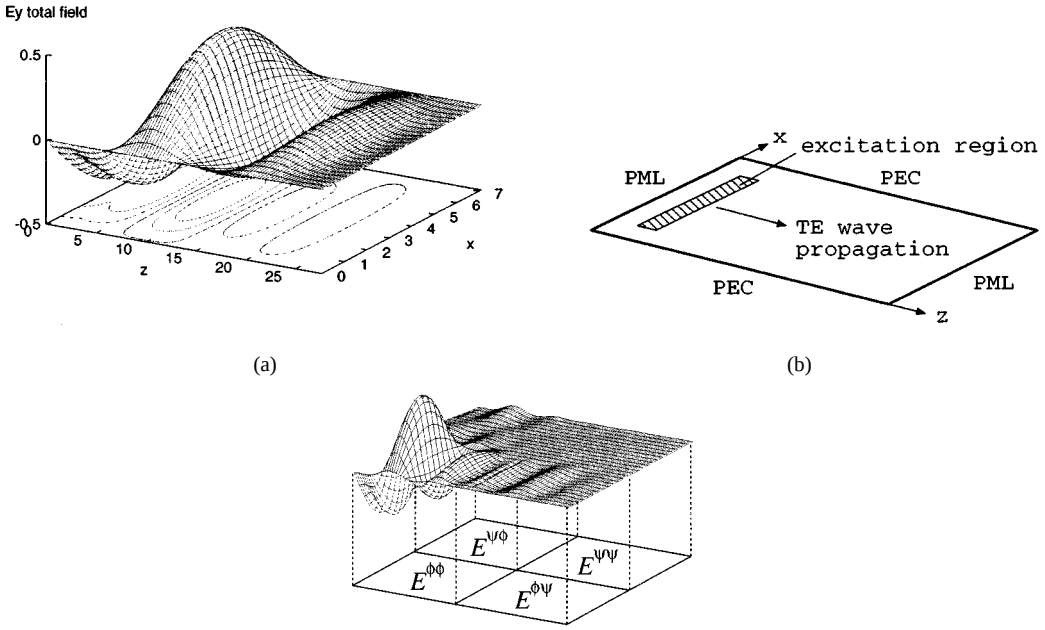


Fig. 6. Decomposition of the $E_y$ field distribution for the $\mathrm{TE}_{10}$ mode propagating in the WR-28 waveguide section. (a) Total $E_y$ field. (b) Geometry of the waveguide section. (c) Wavelet decomposition of the total $E_y$ field into the 2-D Haar basis functions. In (c), each of the four quadrants associated with the basis function coefficients $E^{\phi\phi}$, $E^{\phi\psi}$, $E^{\psi\phi}$, and $E^{\psi\psi}$ covers the entire waveguide section depicted in (a) and (b).

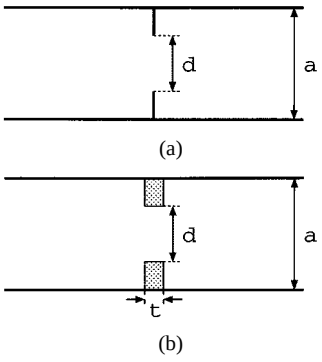


Fig. 7. Top view of the inductive irises in WR-28 waveguide. $a = 7.112$ mm, $d = a/2$, and $t = a/6$. (a) Thin iris. (b) Thick iris.

## III. Application to Waveguide Analysis

TD-Haar modeling was first applied to a simple WR-28 waveguide, then to the WR-28 waveguides containing discontinuities such as thin and thick inductive irises, and finally to iris-coupled waveguide filters. The waveguides in this paper were all terminated with eight-layer Berenger's PML absorbing boundaries [9]. The implementation of the PML boundary conditions is straightforward because it is implemented for each basis function individually, as in the standard FDTD method. It must be noted that the PEC or PMC boundaries for the waveguide sidewalls are enforced even in the PML region.

### A. Simple Rectangular Waveguide

A simple WR-28 rectangular waveguide was first analyzed to demonstrate the decomposition of the total field into the 2-D basis functions $\phi\phi$, $\phi\psi$, $\psi\phi$, and $\psi\psi$. The distributions of the total $E_y$ field are plotted in Fig. 6, together with the coefficients

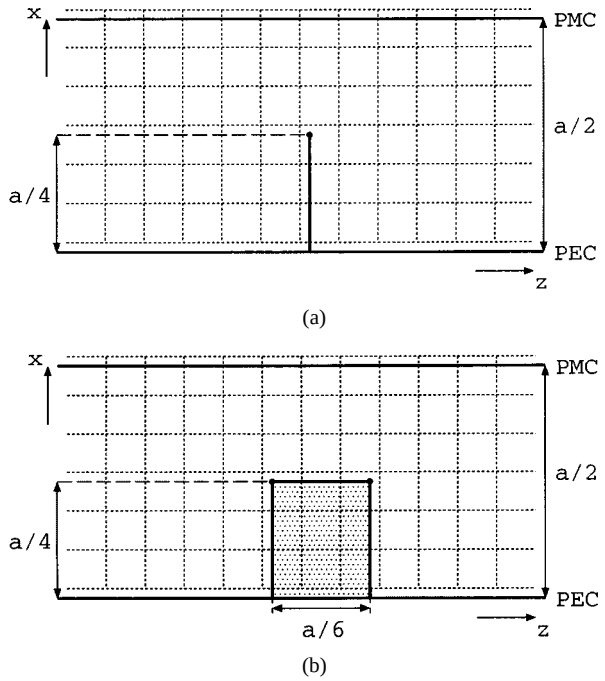


Fig. 8. Discretization of the inductive irises in WR-28 waveguide. Thin lines represent Yee grid lines and thick lines represent the waveguide walls. (a) Thin iris. (b) Thick iris.

$E^{\phi\phi}$, $E^{\phi\psi}$, $E^{\psi\phi}$, and $E^{\psi\psi}$ from which the total $E_y$ field is reconstructed.

It is noted that, in Fig. 6, the major part of the field is represented by $E^{\phi\phi}$, and that the magnitude of $E^{\psi\psi}$ is much smaller than $E^{\phi\phi}$. Note also that the zero tangential electric field at the PEC boundary is achieved through the superposition of the four basis function coefficients.

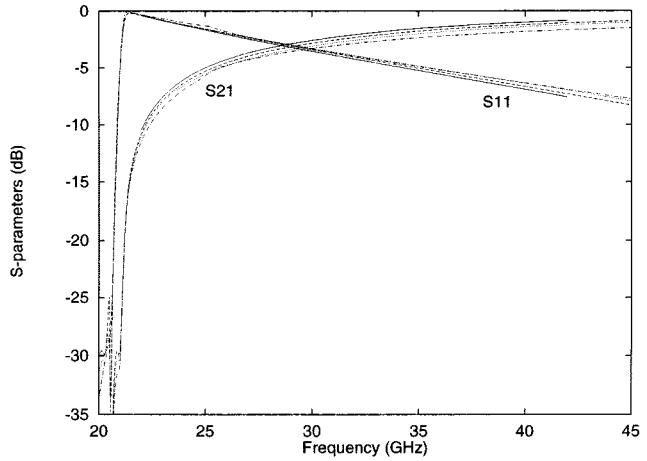


(a)

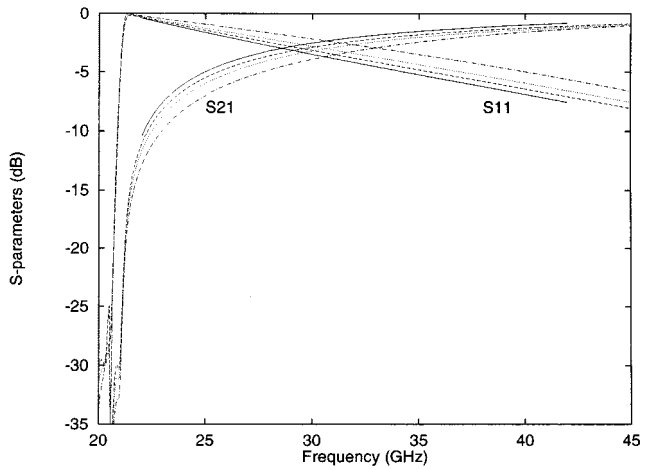


(b)

Fig. 9. $S$-parameters for the thin iris in a WR-28 waveguide obtained: (a) with field-singularity correction and (b) without correction. —: Marcuvitz's equivalent-circuit approximation. - - -: $\Delta x = \Delta z = a/48$. $\cdots\cdots$: $\Delta x = \Delta z = a/24$. - · - · -: $\Delta x = \Delta z = a/12$.

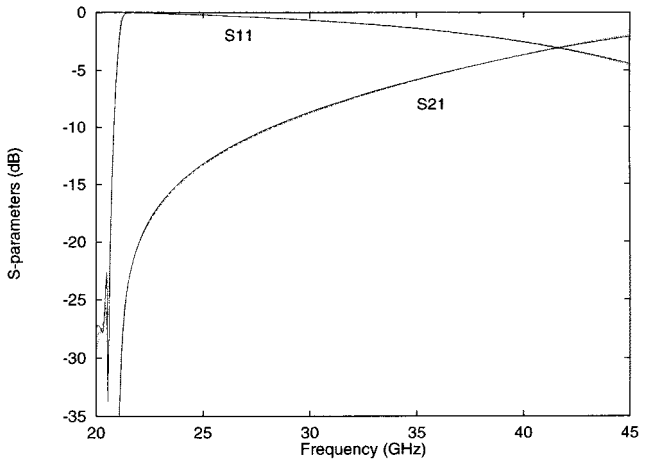


(a)

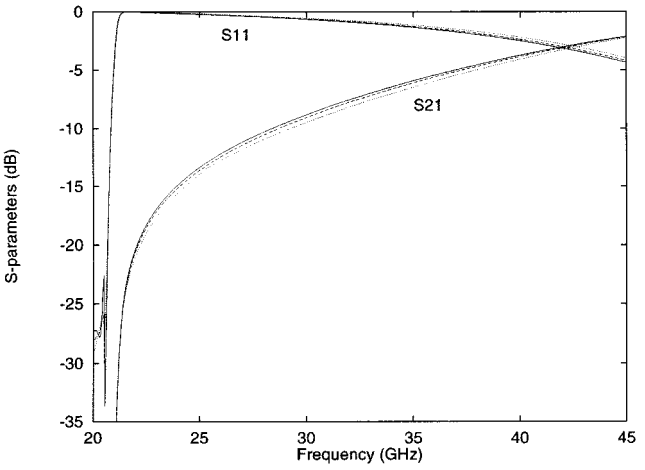


(b)

Fig. 10. $S$-parameters for the thick iris in a WR-28 waveguide obtained: (a) with field-singularity correction and (b) without correction. —: ($\Delta x = a/48$, $\Delta z = a/51$). - - -: ($\Delta x = a/24$, $\Delta z = a/27$). $\cdots\cdots$: ($\Delta x = a/12$, $\Delta z = a/15$).

### *B. Waveguides with Inductive Irises*

Waveguides with thick and thin inductive irises [12] were analyzed with and without the field-singularity correction. The configuration and the discretization of the waveguides are depicted in Figs. 7 and 8, respectively. A PMC wall was placed along the longitudinal center of symmetry of the waveguide to reduce the analysis region by half. Three different discretizations were applied to each structure and convergence of the resulting $S$-parameters was examined. For the thin iris, the grid intervals were $\Delta x = \Delta z = a/12$, $a/24$, and $a/48$, while for the thick iris, $(\Delta x, \Delta z) = (a/12, a/15)$, $(a/24, a/27)$, and $(a/48, a/51)$, where the width of the waveguide $a = 7.112$ mm.

The $S$-parameters of the waveguides obtained by the TD-Haar modeling are shown in Figs. 9 and 10. For the thin iris structure, the frequency response was also obtained by Marcuvitz's equivalent-circuit approximation [13], which, in this case, has a tolerance of less than 1% in magnitude or 0.086 dB. The equivalent-circuit approximation for the thick iris is not demonstrated here because the approximation error is not provided in [13].

In Figs. 9 and 10, one can see that, as the discretization becomes finer, the $S$-parameters converge to a certain values. The convergence is better when the field-singularity correction is implemented in the analysis.

### *C. Iris Coupled Waveguide Filter—Thin Irises*

A waveguide filter with infinitely thin irises [12] shown in Fig. 11 was analyzed. In order to discretize the structure accurately, the grid interval was chosen to be $a/96$ in the direction of the width $a$ of the waveguide, where $a = 7.112$ mm. The distance between the outer iris and PML absorbing boundary condition (ABC) was chosen to be $2a$. The grid interval along the length of the waveguide was 0.0875 mm. A PMC wall was placed across the longitudinal center of symmetry of the waveguide and the total number of Yee cells was $48 \times 642$.

Note that the grid employed for this case is considerably fine simply due to the accurate discretization of the structure. By using a nonuniform grid scheme, much coarser discretization is available; hence, taking advantage of the improvement of computational efficiency through the TD-Haar modeling technique.

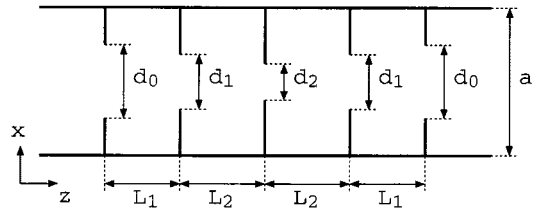


Fig. 11. Top view of iris coupled WR-28 waveguide filter. $a = 7.112$ mm, $d_0 = a/2$, $d_1 = a/4$, $d_2 = a/6$, $L_1 = 4.90$ mm, and $L_2 = 5.595$ mm.

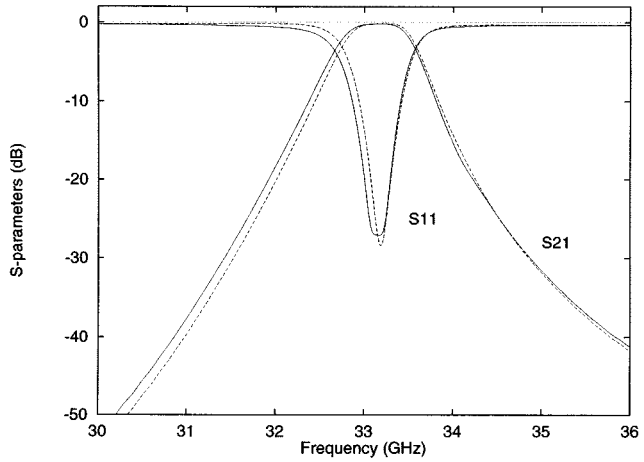


Fig. 12. $S$-parameters for the waveguide filter consisting of thin irises. —: with field-singularity correction. - - -: without field-singularity correction.

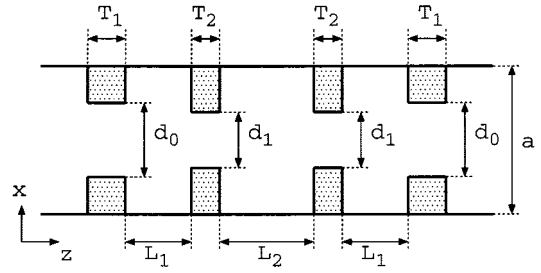


Fig. 13. Top view of the iris coupled WR-28 waveguide filter. $a = 7.0702$ mm, $d_0 = 3.6018$, $d_1 = 2.4$, $L_1 = 4.169$, $L_2 = 4.702$ mm, $T_1 = 1.434$ mm, and $T_2 = 1.1$ mm.

This structure was analyzed with and without the field-singularity correction at the edges of the irises, and the resulting $S$-parameters are shown in Fig. 12. Even with the present discretization, the field-singularity correction makes a slight corrective frequency shift in the $S$-parameters. The CPU time was about 3 h. To obtain the same accuracy without the field-singularity correction, one would need a finer discretization, leading to a longer computation.

### D. Iris Coupled Waveguide Filter—Thick Irises

A waveguide filter consisting of thick irises shown in Fig. 13 was then analyzed. Uniform square grids were used in the analysis, and the grid interval was chosen to be $a/106$ or 0.0667 mm. A PMC wall was placed across the longitudinal center of symmetry of the waveguide. The total number of Yee cells was $53 \times 443$. Due to the restriction of the uniform grids, the filter configuration is not exactly identical to the original design [14], [15]. The maximum discretization error occurred at the outer irises, and was 3%.

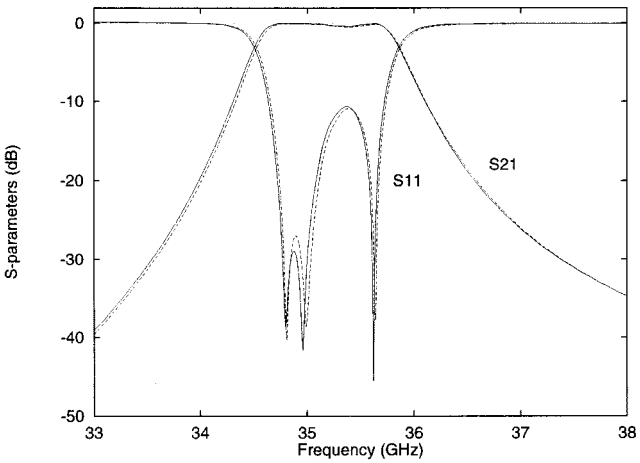


Fig. 14. $S$-parameters for the waveguide filter consisting of thick irises. —: with field-singularity correction. - - -: without field-singularity correction.

TABLE I
CALCULATION CONDITIONS FOR THE WAVEGUIDE PERTURBED BY A THIN IRIS

| $\Delta x = \Delta z =$ | $a/12$ | $a/24$ | $a/48$ |
|---|---|---|---|
| # of Yee cells | 6×48 | 12×96 | 24×192 |
| Time steps | 8480 | 16960 | 33920 |
| CPU time (s) | 10 | 64 | 555 |

This structure was again analyzed with and without the field-singularity correction at the corners of the irises. The resulting $S$-parameters are shown in Fig. 14. The discretization error caused a frequency shift by about 200 MHz for the second dip. However, this problem can be overcome by an accurate discretization using nonuniform grids. The field-singularity correction has resulted again in a slight corrective frequency shift in the resulting $S$-parameters.

### E. Discussion

These results indicate that field-singularity correction enables much faster convergence in the TD-Haar modeling technique. Even in the case of 0° edges, which have the strongest singular fields, the $S$-parameters converge well. For the 90° corner, excellent convergence was obtained; the $S$-parameters obtained with the various discretization levels agree within 0.2 dB when the field singularity is corrected. When analyzing waveguide filters, even though the discretization is relatively fine, the field-singularity correction results in a slight corrective frequency shift in the computed $S$-parameters.

The CPU time for the analysis of the waveguides perturbed by the thin iris is summarized in Table I. The computation was done on a Sun Ultra-5 workstation with 275-MHz clock rate and 256 MB of memory. As the discretization becomes finer, the number of floating point operations increases dramatically and, thus, so does the CPU time. Since the CPU time for the field-singularity correction is negligible compared to the total CPU time, the implementation of the field-singularity correction is highly efficient.

## IV. Conclusions

A 2-D TD-Haar modeling technique with field-singularity correction at sharp metal corners has been presented for the TE polarization case. Various boundary conditions were implemented to analyze waveguide problems. It was found that the field-singularity correction based on quasi-static field approximation was effective in the TD-Haar technique. The field-singularity correction allows us to use coarser discretization and the Haar-wavelet modeling improves accuracy, especially when the discretization is coarse. Faster convergence and better accuracy of the $S$-parameters were achieved when the field singularity was corrected.

## References


[1] M. Krumpholz and L. P. B. Katehi, "New prospects for time domain analysis," *IEEE Microwave Guided Wave Lett.*, vol. 5, pp. 382–384, Nov. 1995.

[2] ——, "MRTD: New time-domain schemes based on multiresolution analysis," *IEEE Trans. Microwave Theory Tech.*, vol. 44, pp. 555–571, Apr. 1996.

[3] M. Werthen and I. Wolff, "A novel wavelet based time domain simulation approach," *IEEE Microwave Guided Wave Lett.*, vol. 6, pp. 438–440, Dec. 1996.

[4] ——, "A wavelet-based time-domain moment method for the analysis of three-dimensional electromagnetic fields," in *IEEE MTT-S Int. Microwave Symp. Dig.*, 1998, pp. 1251–1254.

[5] Y. W. Cheong, Y. M. Lee, K. H. Ra, J. G. Kang, and C. C. Shin, "Wavelet–Galerkin scheme of time-dependent inhomogeneous electromagnetic problems," *IEEE Microwave Guided Wave Lett.*, vol. 9, pp. 297–299, Aug. 1999.

[6] M. Aidam and P. Russer, "Application of biorthogonal B-spline-wavelets to telegrapher's equations," in *Proc. 14th Annu. Rev. Progress Appl. Comput. Electromag. Conf.*, Monterey, CA, Mar. 1998, pp. 983–990.

[7] M. Fujii and W. J. R. Hoefer, "Formulation of a Haar-wavelet-based multi-resolution analysis similar to the 3-D FDTD method," in *IEEE MTT-S Int. Microwave Symp. Dig.*, 1998, pp. 1393–1396.

[8] ——, "A three-dimensional Haar-wavelet-based multiresolution analysis similar to the FDTD method—derivation and application," *IEEE Trans. Microwave Theory Tech.*, vol. 46, pp. 2463–2475, Dec. 1998.

[9] J. P. Berenger, "A perfectly matched layer for the absorption of electromagnetic waves," *J. Comput. Phys.*, vol. 114, pp. 185–200, Oct. 1994.

[10] G. Mur, "The modeling of singularities in the finite-difference approximation of the time-domain electromagnetic-field equations," *IEEE Trans. Microwave Theory Tech.*, vol. MTT-29, pp. 1073–1077, Oct. 1981.

[11] M. Fujii and W. J. R. Hoefer, "Numerical dispersion in Haar-wavelet based MRTD scheme—comparison between analytical and numerical results," in *Proc. 15th Annu. Rev. Progress Appl. Comput. Electromag. Conf.*, Mar. 1999, pp. 602–607.

[12] L. Cascio, G. Tardioli, T. Rozzi, and W. J. R. Hoefer, "A quasi-static modification of TLM at knife edge and $90^{\circ}$ wedge singularities," *IEEE Trans. Microwave Theory Tech.*, vol. 44, pp. 2519–2524, Dec. 1996.

[13] N. Marcuvitz, *Waveguide Handbook*. Boston, MA: Boston Tech., 1964.

[14] W. Menzel *et al.*, "Analysis of a millimeter-wave filter using transmission line matrix and mode matching methods and comparison with measurements," in *Proc. 9th Annu. Rev. Progress Appl. Comput. Electromag. Conf.*, Monterey, CA, Mar. 1993, pp. 289–296.

[15] C. Eswarappa and W. J. R. Hoefer, "Autoregressive (AR) and autoregressive moving average (ARMA) spectral estimation techniques for faster TLM analysis of microwave structures," *IEEE Trans. Microwave Theory Tech.*, vol. 42, pp. 2407–2411, Dec. 1994.



**Masafumi Fujii** (S'97–M'99) was born in Osaka, Japan, in 1966. He received the B.E. and M.E. degrees in electrical and electronic engineering from Kobe University, Kobe, Japan, in 1989 and 1991, respectively, and the Ph.D. degree from the University of Victoria, Victoria, BC, Canada, in 1999.

From 1991 to 1998, he was with the Sumitomo Metal Industries, Ltd., Osaka, Japan, where he was involved in numerical analysis and measurement of microwave components. He is currently a Post-Doctoral Research Fellow in the Department of Electrical and Computer Engineering, University of Victoria. His research interest is in the area of numerical analysis and modeling of electromagnetic fields using wavelets.

**Wolfgang J. R. Hoefer** (M'71–SM'78–F'91) received the Dipl.-Ing. degree in electrical engineering from the Technische Hochschule Aachen, Aachen, Germany, in 1965, and the D.Ing. degree from the Universitaire de Technologie de Grenoble, Grenoble, France, in 1968.

From 1968 to 1969, he was a Lecturer at the Institut Universitaire de Technologie de Grenoble, and a Research Fellow at the Institut National Polytechnique de Grenoble, Grenoble, France. In 1969, he joined the Department of Electrical Engineering, University of Ottawa, Ottawa, ON, Canada, where he was a Professor until March 1992. Since April 1992, he has held the NSERC/MPR Teltech Industrial Research Chair in RF Engineering, Department of Electrical and Computer Engineering, University of Victoria, Victoria, BC, Canada, and is a Fellow of the Advanced Systems Institute of British Columbia. During sabbatical leaves in 1976 and 1977, he spent six months with the Space Division of AEG-Telefunken (now ATN), Backnang, Germany, and six months with the Electromagnetics Laboratory, Institut National Polytechnique de Grenoble. From 1984 to 1985, he was a Visiting Scientist at the Space Electronics Directorate, Communications Research Center, Ottawa, ON, Canada. From 1990 to 1991, he spent a third sabbatical year as a Visiting Professor at the Universities of Rome Tor Vergata, Rome, Italy, Nice-Sophia Antipolis, Nice-Sophia, France, and TUM, Munich, Germany. His research interests include numerical techniques for modeling electromagnetic fields and waves, computer-aided design (CAD) of microwave and millimeter-wave circuits, microwave measurement techniques, and engineering education. He is the co-founder and Managing Editor of the *International Journal of Numerical Modeling*.

Dr. Hoefer is Chair of the IEEE Microwave Theory and Techniques Society (IEEE MTT-S) MTT-15 Technical Committee on Microwave Field Theory. He was an associate editor for the IEEE TRANSACTIONS ON MICROWAVE THEORY AND TECHNIQUES.